Available online at www.sciencedirect.com
SCIENCE DIRECT®
International Journal of Heat and Mass Transfer 47 (2004) 5463–5476
International Journal of HEAT and MASS TRANSFER
www.elsevier.com/locate/ijhmt

# Computations of film boiling. Part II: multi-mode film boiling

Asghar Esmaeeli *, Grétar Tryggvason

*Mechanical Engineering Department, Worcester Polytechnic Institute, Worcester, MA 01609, USA*

Received 15 September 2003; received in revised form 9 July 2004
Available online 23 September 2004

**Abstract**

Film boiling on horizontal periodic surfaces is investigated by direct numerical simulations. A front tracking/finite difference technique is used to solve the momentum and the energy equations in both phases and to account for inertia, viscosity, and surface deformation. Effect of the unit cell size $W$ on the interface dynamics, heat transfer, and fluid flow is studied for different wall superheats. The simulations are carried out over sufficiently long times to capture several bubble release cycles and to evaluate the quasi steady-state Nusselt number $\overline{\langle Nu \rangle}$. While instantaneous Nusselt number will change as result of a change in the system size, statistically steady-state Nusselt number remains almost the same. Simulations of two-dimensional systems in large unit cells, $5\lambda_{d2} < W < 10\lambda_{d2}$, show a distribution of bubble spacing in the range of $0.61\lambda_{d2}$–$1.46\lambda_{d2}$. At relatively low superheats ($Ja \leqslant 0.064$) the bubbles are released periodically from the vapor film, but at intermediate superheats ($0.064 < Ja < 2.13$) permanent vapor jets are formed with no bubble break off. At sufficiently high superheats, the vapor jets start to interact. It is shown that the average bubble spacing does not change with changes in the wall superheat.


## 1. Introduction

In part I of this study [1], we presented a front tracking/finite difference technique for direct numerical simulations of boiling flows. There, the mathematical formulation of the method was presented, the numerical technique was discussed, and the method was validated by comparing our results with the solutions of a few analytical problems and a grid refinement study for film boiling.

Here, we are interested in film boiling on horizontal surfaces where a thin vapor layer covers a heated plate and phase change takes place at the liquid/vapor interface. Although nucleate boiling is usually the more desirable mode of boiling, film boiling continues to be the focus of many boiling studies because it is frequently encountered in industrial applications. In the cryogenic industry, for example, cryogenic fluids are apt to undergo film boiling due to their low boiling points. Other applications include spray cooling of highly heated surfaces, such as those in steel mills, where due to the large superheat film boiling rather than nucleate boiling is dominant.

The individual parameters that govern film boiling are the thermophysical properties of the liquid and the vapor; $\rho_i$, $\mu_i$, $k_i$ $c_i$; $i = l, v$; the buoyancy force $(\rho_l - \rho_v)g$, the wall superheat $\Delta T = T_w - T_{sat}$ (or, the wall heat flux $q_w$), the surface tension $\sigma$ and

* Corresponding author. Tel.: +1 508 831 5462; fax: +1 508 831 5680.
*E-mail address:* aesmae@wpi.edu (A. Esmaeeli).

0017-9310/$ - see front matter © 2004 Elsevier Ltd. All rights reserved.
doi:10.1016/j.ijheatmasstransfer.2004.07.028

**Nomenclature**

| | |
|---|---|
| $A$ | Atwood number (also area), $\frac{(\rho_l-\rho_v)}{(\rho_l+\rho_v)}$ |
| $Nu$ | instantaneous Nusselt number |
| $\langle Nu\rangle$ | space-averaged Nusselt number |
| $\overline{\langle Nu\rangle}$ | time- and space-averaged Nusselt number |
| $Gr$ | the Grashof number, $\frac{\rho_v(\rho_l-\rho_v)gl_s^3}{\mu_v^2}$ |
| $Ja$ | the Jacob number, $\frac{c_v(T_w-T_{sat})}{h_{fg}}$ |
| $Pr$ | the Prandtl number, $\frac{\mu_v c_v}{k_v}$ |
| $Re$ | the Reynolds number |
| $h$ | enthalpy (also convection heat transfer coefficient) |
| $k$ | thermal conductivity |
| $\bar{n}$ | unit normal to the interface (pointing toward the vapor) |
| $T$ | temperature |
| $t$ | time |
| $\bar{u}$ | velocity |

*Greek symbols*

| | |
|---|---|
| $\lambda$ | wavelength |
| $\kappa$ | curvature |
| $\mu$ | dynamic viscosity |
| $\nu$ | kinematic viscosity |
| $\rho$ | density |
| $\sigma$ | surface tension |
| $\tau$ | bubble release period |

*Subscripts*

| | |
|---|---|
| d | most unstable |
| d2 | most unstable two-dimensional |
| d3 | most unstable three-dimensional |
| l | liquid |
| v | vapor |
| $fg$ | (vapor–liquid) |
| sat | saturation |
| c | critical |
| w | wall |
| o | operational condition |
| o,c | operational condition and based on the critical wavelength |
| o,d2 | operational condition and based on the most unstable wavelength |
| B | Berenson |
| K | Klimenko |

*Superscript*

| | |
|---|---|
| $\sim$ | nondimensional |

the latent heat of evaporation $h_{fg}$. Nondimensionalization of these parameters leads to $Gr = \rho_v g(\rho_l-\rho_v)l_s^3/\mu_v^2$, $Ja = c_v\Delta T/h_{fg}$ (or, $Ja = q_w/\rho_g u_s h_{fg}$), $Pr = \mu_v c_v/k_v$, and the ratio of material properties $\rho_v/\rho_l$, $\mu_v/\mu_l$, $c_v/c_l$, and $k_v/k_l$ as the governing nondimensional parameters. Here, $Gr$, $Pr$, and $Ja$ are the Grashof number, the Prandtl number, and the Jacob number. $l_s = \sqrt{\sigma/(\rho_l-\rho_v)g}$ is a capillary length which is used as a characteristic length. Similarly, $u_s = \sqrt{l_s g}$ and $t_s = \sqrt{l_s/g}$ are characteristic velocity and time, respectively. Notice that the two-dimensional critical and the most unstable Taylor inviscid wavelength are related to $l_s$ through $\lambda_c = 2\pi l_s$ and $\lambda_{d2} = 2\pi\sqrt{3}l_s$. The Nusselt number is the most important dependent parameter and is defined as $Nu = -(l_s/\Delta T)\partial T/\partial y|_w$ or $Nu = l_s q_w/k_v\Delta T$, depending on whether the wall superheat or heat flux is controlled, respectively.

Two of the most widely used correlations for the heat transfer coefficient in film boiling on horizontal surfaces are those due to Berenson [3] and Klimenko and Klimenko and Shelepen [4,5]. Berenson's analysis was based on Zuber's model [2] who proposed that the interface behaves as a Taylor wave of wavelength $\lambda_c \leqslant \lambda \leqslant \lambda_{d2}$. Berenson assumed that hydrodynamic instability results in breakup of the waves in a regular pattern with the distance between the bubbles being equivalent to the most unstable wavelength $\lambda_{d2}$. He further assumed that a vapor film of uniform thickness connects the vapor domes and that the vapor generated at the interface flows slowly toward the domes. Thus, he was able to derive a correlation for laminar film boiling near minimum heat flux which in nondimensional form reads

$$Nu_B = 0.425(GrPr/Ja)^{1/4}. \tag{1}$$

Klimenko derived a correlation for both laminar ($Gr \leqslant 4.03\times 10^5$) and turbulent ($Gr > 4.03\times 10^5$) regime using Reynolds analogy and assuming the same cell pattern. Klimenko's correlation is

$$Nu_K = CGr^n Pr^m f_K \tag{2}$$

where $C = 0.19$, $n = 1/3$, $m = 1/3$, and $f_K = f_l$ for laminar flow and $C = 0.0216$, $n = 1/2$, $m = 1/3$, and $f_K = f_t$ for turbulent flow. $f_K$ is given by

$$f_l = \begin{cases} 0.89Ja^{-1/3}, & Ja < 0.71 \\ 1, & Ja \geqslant 0.71 \end{cases};$$

$$f_t = \begin{cases} 0.71Ja^{-1/2}, & Ja < 0.50 \\ 1, & Ja \geqslant 0.50 \end{cases}$$

Klimenko's correlation is believed to correlate most experimental data with an accuracy of ±25% [5].

The main purposes of the current investigation is to shed some light on multimode film boiling where the evolution of the phase boundary leads to formation of bubbles of different sizes and spacings. This can happen if the surface size $W$ is sufficiently large compared with $\lambda_d$ to allow small scale random protrusions at the phase boundary (which are present in practical applications) to grow. We are motivated by the fact that heat removal from a surface is dependent on the bubble generation rate and, therefore, competition between these waves is likely to lead to results different than those due to the evolution of a single-wave. We are interested in a quasi statistically steady-state, after the initial transient, when the Nusselt number has converged to—or fluctuates around—a fixed value, but before all the liquid evaporates. For this problem, Experimental photographs of film boiling on horizontal cylinders and wires can be found in, for example, Lienhard and co-workers [9,10] and Abadzic and Goldstein [14], and a graphical sketch of bubble sites is included in Hosler and Westwater [6] for film boiling on a horizontal plate. We also address the effect of the wall superheat on the results as this parameter is an important controlling factor in industrial applications.

## 2. Choice of fluid and wall superheat

In film boiling of common liquids, the vapor film is usually very thin. If a uniform grid is chosen to accurately resolve the film, the computational cost will be very high and in some cases may be prohibitive. One way to get around this problem is to use a subgrid model where the computational domain is divided into a micro (inside the film) and a macro region (outside the film). While the original governing equations are solved in the macro region using a relatively coarse grid, simplified equations (i.e., boundary layer type) are used in the micro region. Son et al. [15], for example, used this approach to study nucleate boiling with a microlayer. Another approach is to use a nonuniform grid where the grid points are clustered inside the film but a relatively coarse grid is used outside the film. For this study we implemented the latter [1]. Although this enabled us to resolve thin films, the computations cost was still high because the size of the time step $\Delta t$ is determined by the size of the smallest grid block and also because the iterative procedure used to solve the pressure equation (i.e., Eq. (23) in [1]) convergences slower when a nonuniform grid is used. While we carry out a few calculations using the nonuniform grid in this paper, we use uniform grids for most of our calculations, facilitating simulations that must be carried out in large domains and for long times. This is accomplished by using a relatively viscous fluid which results in a thicker film. Thus, the thermophysical properties used in this study are chosen close to those of saturated water at $p_{sat} = 169$ bar (Table 1), except for the Grashof number which is $Gr = 17.85$ in most of our simulations. The lower Grashof number implies a more viscous fluid or an acceleration higher than the normal gravitational acceleration (such as that in a rocket engine). We shall address the effect of $Gr$ on our results in Section 3.5. The length scale, velocity scale, and time scale associated with this choice of fluid are listed in Table 2.

Once the fluid is selected and the the gravitational acceleration is fixed, the wall heat flux, or the wall temperature, is the only free parameter. For a given system pressure, film boiling can be sustained only if the wall heat flux or temperature is above the Leidenfrost point. The minimum heat flux for film boiling on a heated horizontal surface was first determined by Zuber [2] using hydrodynamic considerations. Later, Berenson [3] modified Zuber's theory by refining some of his assumptions and determining the bubble growth rate from experimental data. Both methodologies, however, resulted in the same expression for the minimum heat flux; $\widetilde{q''}_{min} = CA^{1/2}$, with the only difference being a slightly different value for the lead coefficient; $C = \pi/24$ in Zuber's compared with $C = 0.09$ in Berenson's. Here, $\widetilde{q''}_{min} = q''_{min}/\rho_v u_s h_{fg}$ is a nondimensional heat flux and $A = (\rho_l - \rho_v)/(\rho_l + \rho_v)$ is the Atwood number. Berenson also derived a correlation for the minimum wall superheat using the heat convection equation;

Table 1
Properties of water at $p_{sat} = 169$ bar

| $T_{sat}$ | $c/h_{fg}$ | $Pr$ | $Gr$ | $\rho_v/\rho_l$ | $\mu_v/\mu_l$ | $k_v/k_l$ | $c_v/c_l$ |
|---|---|---|---|---|---|---|---|
| 625 K | 0.02 $K^{-1}$ | 4.2 | $36 \times 10^4$ | 0.209 | 0.3857 | 0.281 | 1.726 |

Table 2
Length scales, time scale, and velocity scale used in this study

| $l_s = \sqrt{\sigma/\Delta\rho g}$ | $\lambda_c = 2\pi l_s$ | $\lambda_{d2} = 2\pi\sqrt{3} l_s$ | $t_s = \sqrt{l_s/g}$ | $u_s = \sqrt{l_s g}$ |
|---|---|---|---|---|
| 0.2571 | 1.6154 | 2.798 | 0.3585 | 0.717 |

$\Delta T_{\min} = q''_{\min}/h_{\min}$, $h_{\min}$ being the heat convection coefficient near the minimum heat flux (i.e., $h_{\min} = Nu_B k_v/l_s$). His correlation in nondimensional form yields

$$Ja_{\min} = 0.127(A^2 Re^4 Pr^3/Gr)^{1/3}, \tag{3}$$

where $Ja_{\min} = c_v \Delta T_{\min}/h_{fg}$ is the Jacob number below which film boiling changes to transition boiling and $Re = u_s l_s/\nu_v$ is a Reynolds number based on the characteristic length and velocity scales.

The agreement of the above correlation with experimental results is mixed. While Eq. (3) resulted in a ±10% error for Berenson's own experiments with n-pentane and carbon tetrachloride, the experiments by Hosler and Westwater [6] with water at atmospheric pressure showed that this equation underpredicted their data by more than 50%. On the other hand, Dhir et al. [7] observed in their pseudo-film boiling studies (by sublimation of a dry ice beneath a pool of warm water) that $\Delta T_{\min}$ by Berenson's prediction was about two times larger than that of their experimental result. They attributed this difference to the overprediction of the lead coefficient in Eq. (1) as a result of assuming that bubble would be generated both at the node and the antinode, since they observed that bubbles were generated only at the nodes.

In our simulation, we fix the wall temperature rather than the wall heat flux. Thus, Eq. (3) predicts $Ja_{\min} = 0.4375$ for our set of parameters. We believe that this is an overprediction as we were able to run film boiling simulations at Jacob numbers as low as $Ja = 0.0213$ where evaporation was still sufficiently fast to prevent wetting. While we are interested in examining as broad range of wall superheat as possible, there are restrictions at both high and low values that need to be addressed. Lower superheats result in a thin vapor film that demands very high grid resolutions. At higher superheats (i.e., $\Delta T \geqslant 400\,\mathrm{K}$), on the other hand, radiation effects become important and must be taken into account. To avoid resolving extremely thin films and taking the radiation effects into consideration, we have elected to work with Jacob numbers in the range $0.064 \leqslant Ja \leqslant 2.132$.

## 3. Results

### 3.1. Film boiling in small unit cells

Models of film boiling are generally based on the assumption that regularly spaced bubbles are generated from linearly the most unstable wavelength. Around the maximum growth rate, the growth versus wave number curve is, however, relatively flat. In multimode boiling it is therefore likely that waves of slightly different wave numbers grow also. To examine how waves of different length evolve and what the effect of the wavelength is on the heat transfer and the evaporation rate, we have run two fully three-dimensional simulations with $Ja = 0.064$. In one case we select $W = \lambda_{d3}$ and in the other we take $W = 1.4\lambda_{d3}$. The initially flat phase boundary is perturbed in the following way:

$$z = z_c + \epsilon_x[\cos(2\pi N_x x/W_x) + \sin(\pi N_x x/W_x)] + \epsilon_y[\cos(2\pi N_y y/W_y) + \sin(\pi N_y y/W_y)].$$

For $W = \lambda_{d3}$, we take $z_c = 0.125\lambda_{d3}$, $W_x = W_y = \lambda_{d3}$, $\epsilon_x = 0.018\lambda_{d3}$, $\epsilon_y = 0.036\lambda_{d3}$, and $N_x = N_y = 2$. For $W = 1.4\lambda_{d3}$, we increase $W_x$, $W_y$, $z_c$, $\epsilon_x$, and $\epsilon_y$ by factor of 1.4 but use the same $N_x$ and $N_y$. These initial perturbations consist of two bimodal waves in the $x$ and the $y$ direction. The superposition of these waves results in four unequal humps at the interface. The center of these humps, in a descending order of their heights, are at $(W_x, W_y)$, $(0, W_y)$, $(W_x, 0)$, and $(0, 0)$. Fig. 1a shows the initial phase boundary and the late amplitude stage for $W = \lambda_{d3}$, after the initial perturbation has grown and bubbles have been formed. Fig. 1b shows an intermediate stage and the late amplitude stage for $W = 1.4\lambda_{d3}$. In the first case, the long wave perturbation leads to competition between the waves and only two bubbles are formed. Since the initial growth rate of each hump is proportional to its height, the bubbles that eventually appear are formed from the highest humps. In the second case, where the primary wave is longer than the most unstable wave, all four humps grow to form bubbles.

To find out how the interface evolution influences the heat flux, in Fig. 2 we compare space-averaged Nusselt number, defined as $\langle Nu\rangle = -l_s/(A\Delta T)\int_A \partial T/\partial y|_w \mathrm{d}A$, for these simulation and the single-mode simulation in [1] which was run in a $\lambda_{d3} \times \lambda_{d3} \times 2\lambda_{d3}$ domain and at the same nondimensional numbers. We also include the results of two simulations for two-dimensional systems (which are counterpart of the simulations in Fig. 1) for comparison. Here, $A$ is the surface area. $\langle Nu\rangle$ is initially high because of the large temperature difference between the wall and the vapor. This is, however, an artifact of the initial temperature condition and will not have any effect on the quasi-steady results. Son and Dhir [11], for example, set their initial vapor temperature field using a saturation temperature, a linear profile, and a temperature profile from a steady-state result of a simulation with a coarser grid and found essentially no effect on the time-averaged Nusselt number. The Nusselt number, after decreasing initially, increases again as a bubble is formed and when the film thickness is minimum. $\langle Nu\rangle$ is the same for all the curves up to $t = 1.39$ but starts to deviate as a result of differences in evolution of the phase boundaries. The Nusselt numbers predicted by Berenson's and Klimenko's correlations are also included in

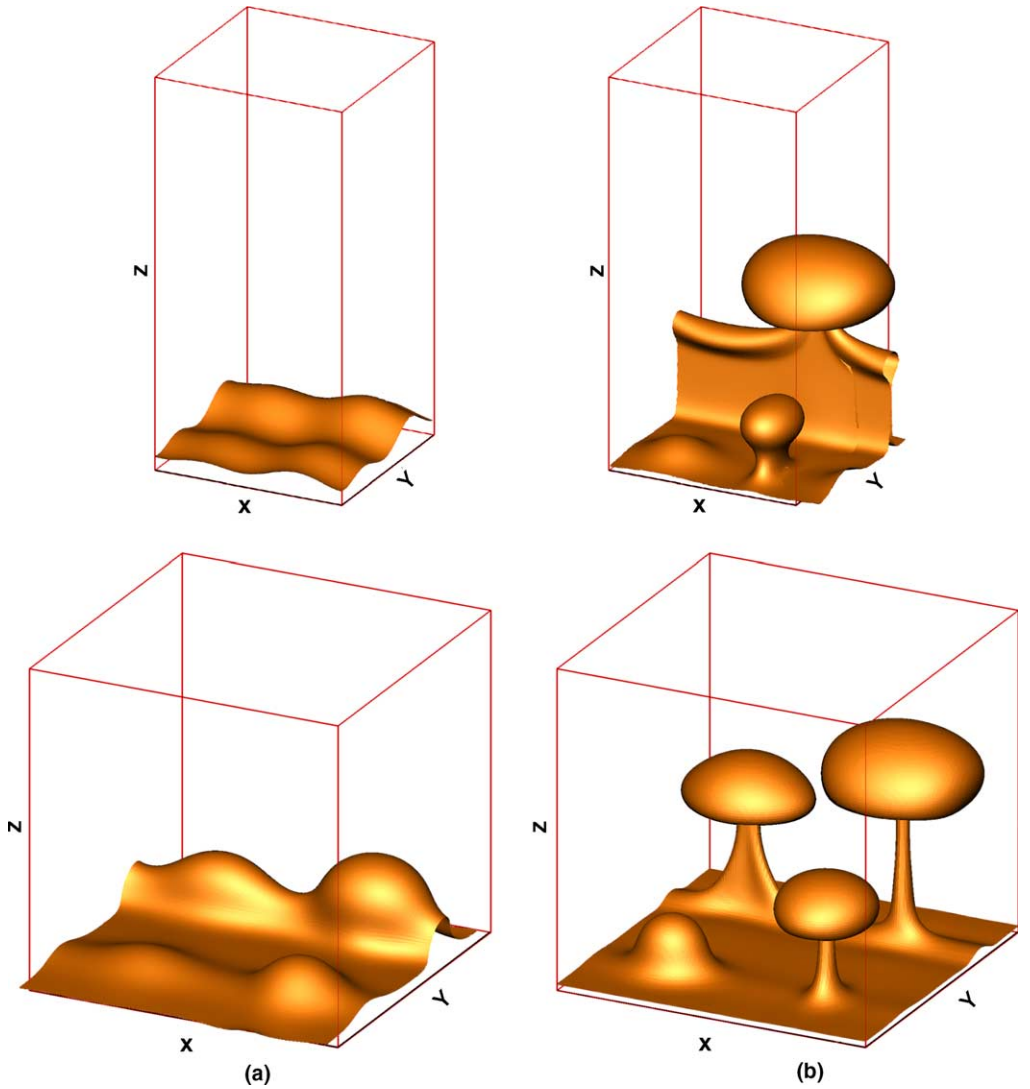


Fig. 1. Evolution of a liquid/vapor interface due to bimodal initial perturbations at $Ja = 0.064$. Except for $Gr = 17.85$, the nondimensional numbers are the same as those listed in Table 1. For the top frames, the domain size is $\lambda_{d3} \times \lambda_{d3} \times 2\lambda_{d3}$, the grid resolution is $96 \times 96 \times 192$ grid, and times are 0 and 13.94. For the bottom frames, the domain size is $1.4\lambda_{d3} \times 1.4\lambda_{d3} \times 1.4\lambda_{d3}$, the grid resolution is $128 \times 128 \times 128$ grid, and times are 6.97, 14.64.

the figure and are in the same range as the numerical results.

### 3.2. Film boiling in large unit cells

To fully address the effect of allowing many modes to interact freely it is necessary to follow the evolution of a significantly larger number of modes. Due to the expense of doing so for a fully three-dimensional flow, we have elected to continue the studies by simulations of two-dimensional systems. The good agreement between experimentally observed heat transfer rates and predictions for two-dimensional systems, shown later, suggests that these simulations capture much of the dynamics. There are of course some differences between the two systems as can be seen by inspection of Fig. 2.

We start our analysis by investigating the evolution of a phase boundary in a $W = 10\lambda_{d2}$ unit cell. The domain height is $2\lambda_{d2}$ and the grid resolution is $1280 \times 256$ points. The interface is initially perturbed by $N = 30$ random waves described by

$$y = y_0 + \epsilon/N \sum_{i=1}^{N} r(i)[\cos(2\pi i x/W) + \sin(2\pi i x/W)],$$

where, $y_0 = 0.125\lambda_{d2}$, $\epsilon = -0.05\lambda_{d2}$, and $0 \leqslant r(i) \leqslant 1$ is a number determined by a random number generator.

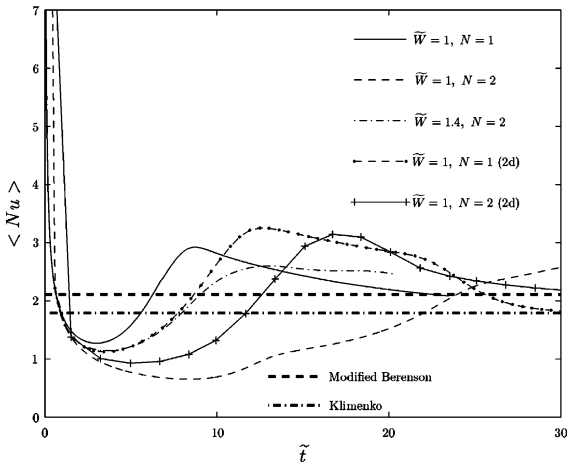


Fig. 2. Evolution of $\langle Nu \rangle$ for a single-mode and bimodal simulations of two- and three-dimensional systems.

We also include another vapor layer on top of the liquid layer to allow rising bubbles to break through. The position of the second interface is at $1.25\lambda_{d2}$. All the nondimensional numbers for this run are the same as those of the previous simulations. The exact mechanism of bubble break off is still being actively investigated, but in our code, we allow the topology to change simply whenever the diameter of the thread connecting the bubble to the base is smaller than two grid spacings. Although changing this criteria may affect the shape of the phase boundary slightly, we have found that the overall statistical results remain essentially the same.

Fig. 3 shows the evolution of the phase boundary. The first frame shows the initial position and the subsequent frames show the interface at selected times noted in the caption. Initially, short wave perturbations are stabilized by surface tension but larger ones are not affected. The interactions between the larger perturbation results in a distribution of waves of different amplitudes as seen in the second frame. As time progresses, the interface becomes more unstable and vapor bulges are formed around the peaks of these waves (frame 3). These bulges are at different stages of growth depending on the their amplitude at time zero. For instance, in the third frame we observe a bubble break off at the fifth and the last sites while the bubble at the fourth site is still in the formation stage. We observe ten bubbles distributed in a width of $10\lambda_{d2}$ which indicates an average of one bubble per $\lambda_{d2}$, just as was the case for the single mode simulation. However, the peak to peak distances is in the range of $0.81\lambda_{d2}$–$1.31\lambda_{d2}$. Frames 4–6 show the formation of three steady jets and some alternate bubble generation at the nodes and antinodes. For example, the bubble generation site marked in the last frame has no counterpart in the fifth frame. However, this is not a dominant feature of this run and an animation of the results showed that most of the bubble generation sites remain the same during the quasi steady-state. A plot of the Nusselt number versus time (i.e., Fig. 4) showed that the quasi steady-state was reached at around $t = 50$–$60$. Thus, the first five frames are representative of the transient evolution while the last frame represents the phase boundary at the quasi steady-state. Comparison of the size of the bubbles in the last frame with those at the earlier times show that the bubbles in the quasi steady-state are smaller than those during the first instant of bubble break off. This is due to the decrease in the average heat flux after the system reaches a steady-state. The bubbles deform after they rise and at the time of coalescence with the top surface they look like ellipses with ratio of minor to major axes in the range 0.18–0.5. Inspection of the sixth frame shows that the bubble spacing at quasi steady-state is in the range of $0.58\lambda_{d2}$–$1.43\lambda_{d2}$. This spacing was measured by marking the permanent jets, active sites, and the sites that most recently released bubbles. Here, the average bubble spacing is $0.913\lambda_{d2}$ which shows that for sufficiently large domains, the dominant bubble spacing is less than the most unstable wavelength. This is in-line with the observations for three-dimensional systems (Fig. 1) where two bubbles were formed per $1.4\lambda_{d3}$ length.

To find out how the number of initial perturbation modes affects the result, we have performed three more simulations in the same domain but with $N = 2$, 5, and 60 random modes. Comparison of the phase boundaries for these runs in quasi steady-state showed a similar average bubble spacing. In the first run, it took a long time for the instability to set in and the bubble release pattern was more irregular. In the second run, the instability set in relatively quickly. In the third run, the small scale perturbations were stabilized very fast and the interface evolution was similar to the original run. Fig. 4 compares $\langle Nu \rangle$ for these runs as well as $\langle Nu \rangle$ for the $N = 30$ run seen in Fig. 3. Although the instantaneous Nusselt numbers are different, time-averaged Nusselt numbers, defined as $\overline{\langle Nu \rangle} = 1/(\Delta t) \int_{t_i}^{t_e} \langle Nu \rangle \mathrm{d}t$ are very close; $\overline{\langle Nu \rangle} = 2.0350$, 2.0037, 2.1483, 2.0966 for $N = 2$, 5, 30, and 60, respectively. Here, $\Delta t = t_e - t_i$, where $t_i$ and $t_e$ are the beginning time of the steady-state and the end-time of the simulation, respectively. The peaks and the valleys in the figure correspond to the times right before bubbles depart (when the average film thickness is minimum) and the times when the average film thickness is relatively high. Once a bubble is released, surface tension pulls the interface back and the process repeats itself. It should be noted that if the wall heat flux $q_w$ is imposed rather than the wall temperature, the wall temperature goes through a similar oscillation. In that case, a Nusselt number defined as $\langle Nu \rangle = (l_s q_w / k_v W) \int_0^W \mathrm{d}x/(T_w - T_{sat})$ will be minimum when the average film thickness is maximum and vice versa, reflecting

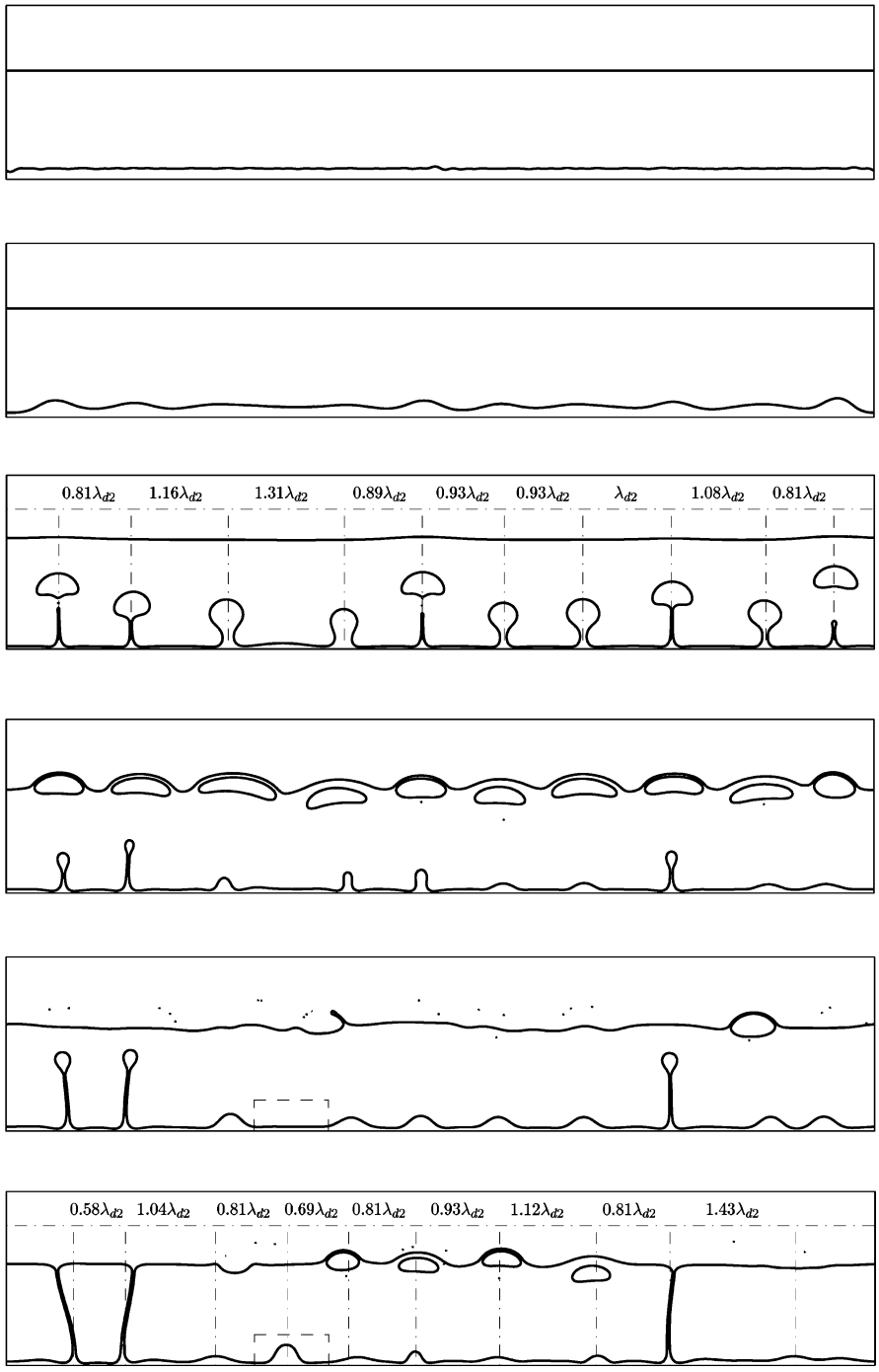


Fig. 3. Evolution of a multimode phase boundary. The initial interface consists of $N = 30$ random waves in a $10\lambda_{d2} \times 2\lambda_{d2}$ domain. The grid resolution is $1280 \times 256$. Here, $Ja = 0.064$ and except for $Gr = 17.85$, the nondimensional numbers are the same as the corresponding ones in Table 1. The frames proceed from the top to the bottom and times are 0, 13.94, 27.89, 41.84, 55.78, and 137.37.

the fact that $T_w$ increases with increase in the average film thickness to compensate for the higher thermal resistance.

The results of a handful of experimental measurements of the bubble spacing are mixed. For example, a photograph by Lienhard and Dhir [9] of film boiling of water form a horizontal wire, shows a uniform bubble spacing of $\lambda_{d2}$, while a two-dimensional sketch of bubbles by Hosler and Westwater [6] shows a

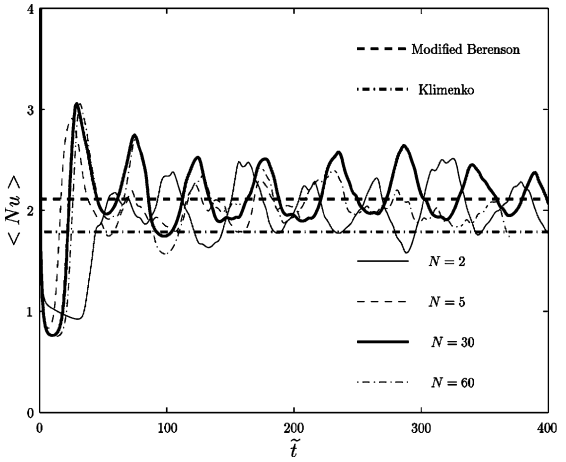


Fig. 4. Comparison of the Nusselt number for multimode simulations with different number of initial waves. The domain size is $10\lambda_{d2} \times 2\lambda_{d2}$ and the grid resolution is $1280 \times 256$.

distribution of bubble spacings with average spacing larger than $\lambda_c$ but very close to $\lambda_{d2}$. Apart from these experimental measurements, the only relevant investigation that we are aware of is a numerical/analytical study of thin viscous films by Yiantsiso and Higgins [12]. Although phase change was not included in this study, their observations lend some support to our findings in the sense that it shows possibility of having a distribution of bubble spacing. To study the long-time behavior of the phase boundary, they found an asymptotic solution for the creeping flow equation in the liquid and lubrication equation in the film. They showed that the interface would approach a sinusoidal wave (i.e., bubble) of length $\hat{\lambda}_{d2} = \sqrt{2/3}\lambda_{d2}$ at a steady-state, while the film thickness between the bubbles became zero. An infinite spectrum of periodic steady-state interfacial shapes was found to be possible. An energy analysis revealed that a state of one bubble per $\hat{\lambda}_{d2}$ was the most energetically favorable. However, the numerical simulations (conducted for two-dimensional systems) indicated that this state may not always be reached. Rather, the number of bubbles formed was determined by the fastest growing mode, while their relative size depended on the initial conditions. The net result of their analysis was that for a periodic domain of size $W$, if $n\hat{\lambda}_{d2} < W < (n+1)\hat{\lambda}_{d2}$, where $n$ is an integer, one could have any number of bubbles between 1 and $n$ with arbitrary heights and spacing, provided of course the total area (volume in three dimensions) was conserved. For the simulations in Fig. 4 $W = 10\lambda_{d2}$ and their analysis predicts formation of one to 12 bubbles. It should be noted that for these simulations the number of bubbles during the transient was always around 10. However, the number of bubbles at quasi steady-state was different.

### 3.3. Effect of the unit cell size

To evaluate the dependency of our results on the size of the unit cell, we have performed three more simulations in smaller, $W = \lambda_{d2}$ and $W = 2\lambda_{d2}$ domains, and a larger, $W = 20\lambda_{d2}$ domain. The height of the computational domain was $2\lambda_{d2}$ in all cases. The grid resolution for the small domains was 128 per $\lambda_{d2}$ and for the large domain it was 64 points per $\lambda_{d2}$. The interface for $W = \lambda_{d2}$ and $W = 2\ \lambda_{d2}$ was perturbed by a single and a two waves, respectively. The interface for the larger simulations was perturbed similarly to that in Fig. 3. For the first case, the bubbles were always released at the site with the maximum initial amplitude. For the second case, the bubbles were released alternately at each site. For the third case, wave interactions led to a similar interface evolution as that seen in Fig. 3, but no permanent vapor jet was formed due to a lower grid resolution. Fig. 5 compares the instantaneous Nusselt number for these runs. In all cases, after a short period, the Nusselt number starts to oscillate as the systems reach a quasi steady-state. The period and amplitude, however, are more irregular for the multimode simulations due to a more random bubble release. The phase differences between the curves indicates the differences in the bubble release period. Although we believe that the simulations have passed well beyond the transient stage, animations of the results showed that the release times of the bubbles are strongly correlated, resulting in the oscillations seen in the figure.

In Fig. 6a we plot $\overline{\langle Nu \rangle}$ versus $\widetilde{W} = W/\lambda_{d2}$ where it is seen that $\overline{\langle Nu \rangle}$ does not vary much with $\widetilde{W}$. This is a good news from a computational point of view, since the Nusselt number computed for a small unit cell may be readily applicable to larger systems used in the

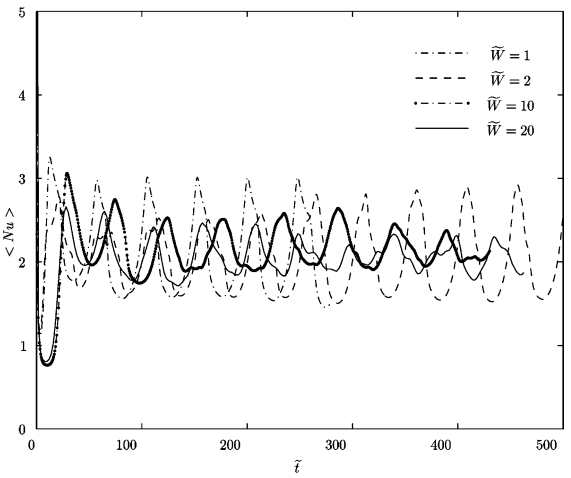


Fig. 5. Nusselt number for different unit cell sizes as a function of time.

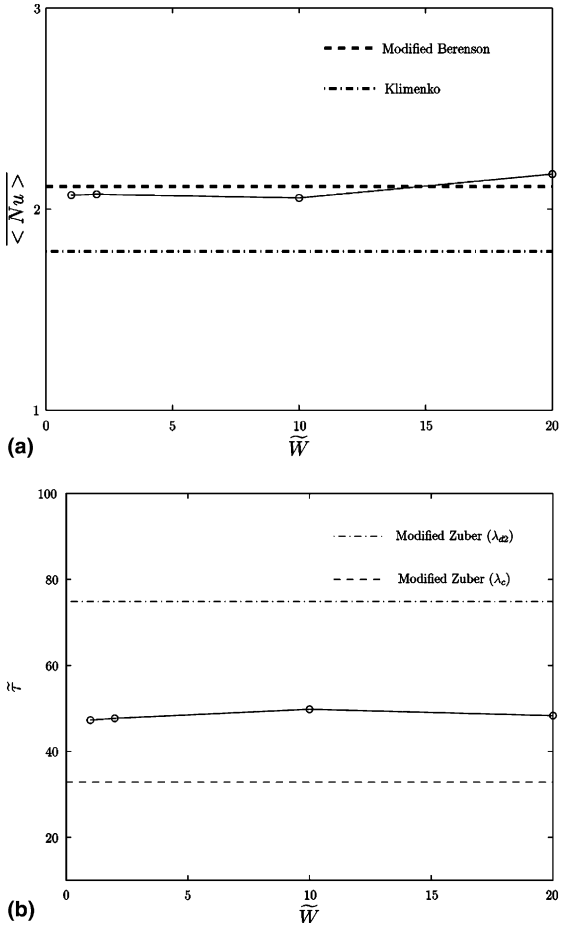


Fig. 6. Quasi steady-state (a) Nusselt number and (b) bubble release period as a function of the unit cell size. Here, $Ja = 0.064$ and except for $Gr = 17.85$, the nondimensional numbers are the same as the corresponding ones in Table 1.

industry. This, however, needs to be verified for three dimensional systems. The Nusselt number for this case using Berenson's correlation and Klimenko's correlation is 2.112 and 1.7892, respectively.

In Fig. 6b we plot the quasi steady-state bubble release period $\tilde{\tau} = \tau/t_s$ as a function of $\widetilde{W}$ where it is seen that $\tilde{\tau}$ is essentially independent of $\widetilde{W}$. Bubble release period for each case is calculated by measuring the peak to peak distances of the corresponding curve in Fig. 5 and taking an average. While the resulting period represents the time between successive release of bubbles from the same site for a single-mode simulation, it is the average of periods over all the sites for multimode simulations, where each site has a different frequency.

Zuber [2] derived a relation for steady-state bubble release period near the minimum heat flux by considering Kelvin–Helmholtz instability of a vertical liquid/vapor interface when fluid velocities and gravity are set to zero. Under these assumptions, the frequency is $n^2 = \sigma k^3/(\rho_v + \rho_l)$ and the critical bubble period $\tau_c = 2\pi/n_c$ follows from inserting for $k_c = 2\pi/\lambda_c$ in the expression for $n^2$. The resulting correlation in nondimensional form is $\tilde{\tau}_{min,c} = 2\pi/\sqrt{A}$. Experimental measurements of Hosler and Westwater [6] showed that Zuber's period correlated best with their data if they replaced $\lambda_c$ with $\lambda_{d2}$ which results in $\tau_{min,d2} = 3^{3/4}\tau_{min,c}$. Zuber's period must be modified when the wall heat flux is different from $q''_{min}$. Here, we take a more general approach and derive a relation for variations of $\tilde{\tau}$ as a function of governing nondimensional parameters $Ja$, $Gr$, and $Pr$. We note that the period is inversely proportional to the wall heat flux; $\tau \sim 1/q''_w$. Therefore, for different wall heat fluxes $\tau_1/\tau_2 = q''_{w,2}/q''_{w,1}$. Since in our simulations the wall superheat (rather than the heat flux) is controlled, we should relate $q''_w$ to $\Delta T$; $\tau_2/\tau_1 = (h_1\Delta T_1)/(h_2\Delta T_2)$. The heat transfer coefficient $h$ is a function of the thermophysical properties, gravitational acceleration, as well as the wall superheat. Any change in one of the above parameters will lead to a change in $h$. While we work with fixed physical properties in most part of the present study, in Section 3.5 we will change viscosities $\mu$ and conductivities $k$ of both phases to investigate the effect of the Grashof number. Therefore, characteristic length, time, and velocity ($l_s$, $t_s$, and $u_s$) will remain unchanged throughout this study. Thus, we can nondimensionalize the above relation in the following way

$$\frac{\tau_2/t_s}{\tau_1/t_s} = \left(\frac{h_1 l_s/k_{v,1}}{h_2 l_s/k_{v,2}}\right)\left(\frac{k_{v,1}}{k_{v,2}}\right)\left(\frac{c_v\Delta T_1/h_{fg}}{c_v\Delta T_2/h_{fg}}\right).$$

Next, we substitute for $hl_s/k$ in terms of $Nu$ and nondimensionalize $k$ as $Pe = \rho_v l_s u_s/k$, where $Pe$ is a Peclet number. This leads to $\tilde{\tau}_2/\tilde{\tau}_1 = (Nu_1/Nu_2)(Pe_2/Pe_1)(Ja_1/Ja_2)$. Finally, we substitute for $Nu$ from Eq. (1) and replace $Pe$ with $Re\,Pr$; $\tilde{\tau}_2/\tilde{\tau}_1 = (Gr_1/Gr_2)^{1/4}(Pr_2/Pr_1)^{3/4}(Ja_1/Ja_2)^{3/4}(Re_2/Re_1)$. This equation suggests that

$$\tilde{\tau} \sim Re\left(\frac{Pr^3}{GrJa^3}\right)^{1/4}, \tag{4}$$

which implies that $\tilde{\tau}$ depends on one extra nondimensional number compared to $Nu$. We note that using a different correlation for $Nu$ such as Klimenko's correlation would lead to a similar result but with different exponents. Eq. (4) can be used to modify Zuber's period for wall superheats different from the minimum wall superheat $\tilde{\tau}_o = \tilde{\tau}_{min}(Ja_{min}/Ja_o)^{3/4}$, where the subscript o stands for the operating condition.

The bubble release period was also determined analytically by Chang [8] who used hydrodynamic instability in conjunction with a solution of a moving liquid/vapor interface (similar to our third validation test in [1]). The thickness of the vapor layer $\delta$ was found (as part of the solution) to be $\delta = 2\sqrt{\alpha_{eq}t}$, where $\alpha_{eq}$ is an

equivalent thermal diffusivity. An approximate solution of the energy jump condition resulted in $\alpha_{eq} = k_v \Delta T / 2 h_{fg} \rho_v$. The stability criteria for the interface was used to determine the critical thickness $\delta_c = (8\pi^2 \mu_v \alpha_{eq}/g\Delta\rho)^{1/3}$ at which the interface will break up. The bubble release period, therefore, corresponds to this critical thickness, i.e., $\tau = \delta_c^2/4\alpha_{eq}$. Inserting for $\delta_c$ and $\alpha_{eq}$ in the expression for $\tau$ and nondimensionalizing results in

$$\tilde{\tau} = (2\pi^4)^{1/3} Re \left( \frac{Pr}{Gr^2 Ja} \right)^{1/3}. \quad (5)$$

Notice that the trend of variations of $\tilde{\tau}$ with the governing nondimensional parameters is the same for Eqs. (4) and (5).

Here, Zuber's modified correlation results in $\tilde{\tau}_{o,c} = 32.83$ and $\tilde{\tau}_{o,d2} = 74.86$, where $\tilde{\tau}_{o,c}$ and $\tilde{\tau}_{o,d2}$ refers to period based on $\lambda_c$ and $\lambda_{d2}$, respectively. As can be seen from Fig. 6b, the time-averaged numerical period falls between $\tilde{\tau}_{o,c}$ and $\tilde{\tau}_{o,d2}$. Chang's correlation, on the other hand, results in $\tilde{\tau} = 7.465$ which is substantially different from our results and Zuber's prediction.

We also computed the Fourier transform of $\overline{\langle Nu \rangle}$ over the interval $\Delta t = t_e - t_i$ for the simulations in Fig. 5. The Fourier transform showed a dominant frequency for each run which corresponded to the bubble release frequency of that run. A plot of the bubble release frequency and the power as a function of $\widetilde{W}$ showed that these quantities are essentially independent of $\widetilde{W}$; confirming the observation made about Fig. 6.

### 3.4. Effect of the wall superheat

An increase in the wall superheat results in an increase in the Jacob number and a decrease in the Nusselt number. For laminar film boiling, Chang [8] and Klimenko [4] predict that $Nu \sim Ja^{-1/3}$, while Berenson [3] and Hamil and Baumeister [13] predict that $Nu \sim Ja^{-1/4}$. However, Klimenko's correlation also predict that $Nu$ will not change beyond $Ja = 0.71$. Experimental studies (see, for example, [14]) show that as the Jacob number increases, the vapor plume gets thicker and it may not readily break into bubbles or break up at all. At sufficiently high superheats, interaction between the jets is observed.

To investigate the effect of the wall superheat on the bubble spacing and evolution of the interface, we have performed five multimode simulations at Jacob numbers of 0.213, 0.427, 0.853, 2.132, and 10.664 with the same initial conditions as used in the multimode run in Fig. 3. Although radiation effects are likely to be important for the last run, we have not taken them into account. The depth of the liquid and the height of the domain for the last two runs were increased to accommodate faster bubble growth. In Fig. 7 we compare the phase boundaries for these runs at a transient time. The figure shows the formation of ten bubbles for each case, and it is immediately obvious that the bubble spacing at this stage is not affected by the change in the wall superheat. Therefore, as has been argued by Zuber [2], the bubble spacing is determined solely by hydrodynamics effects. The figure shows that as the wall superheat increases the bubble size and the width of the vapor jet increases. In Fig. 8 we compare these simulations at late times. The time for the first four frames is $\widetilde{t} = 181.26$ which is in the quasi steady-state regime. The last two simulations are at transient times $\widetilde{t} = 44.62$ and 31.37 and these two systems may not even have a quasi steady-state as a result of rapid depletion of the liquid. While bubbles break off periodically in the first run, the rest of the runs does not show a sustained bubble break off. For $0.064 \leqslant Ja \leqslant 0.853$, steady jets are formed which form bridges

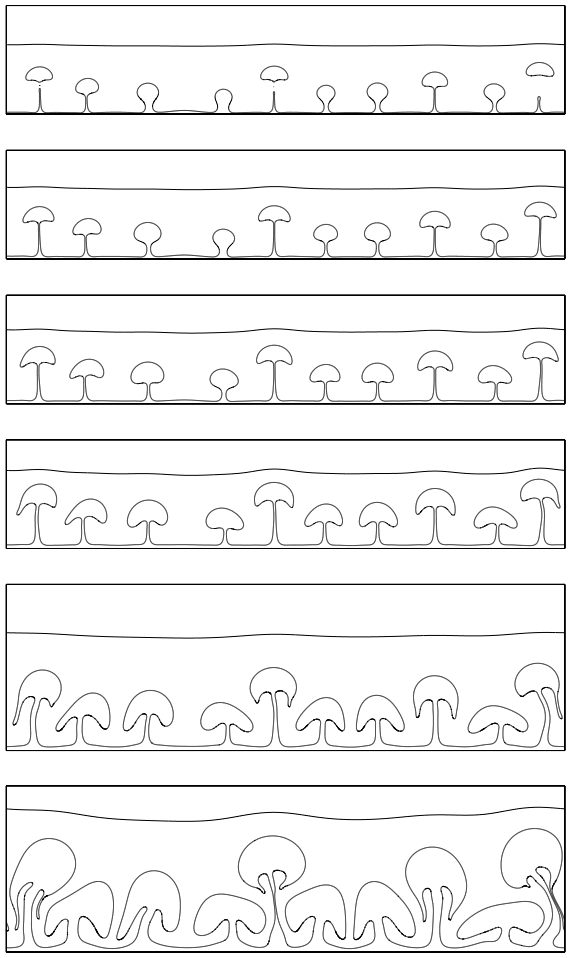

Fig. 7. Comparison of the phase boundaries at $\widetilde{t} = 27.89$ for multimode simulations at Jacob numbers 0.0640, 0.213, 0.427, 0.853, 2.132, and 10.66. The frames proceed from the top to the bottom.

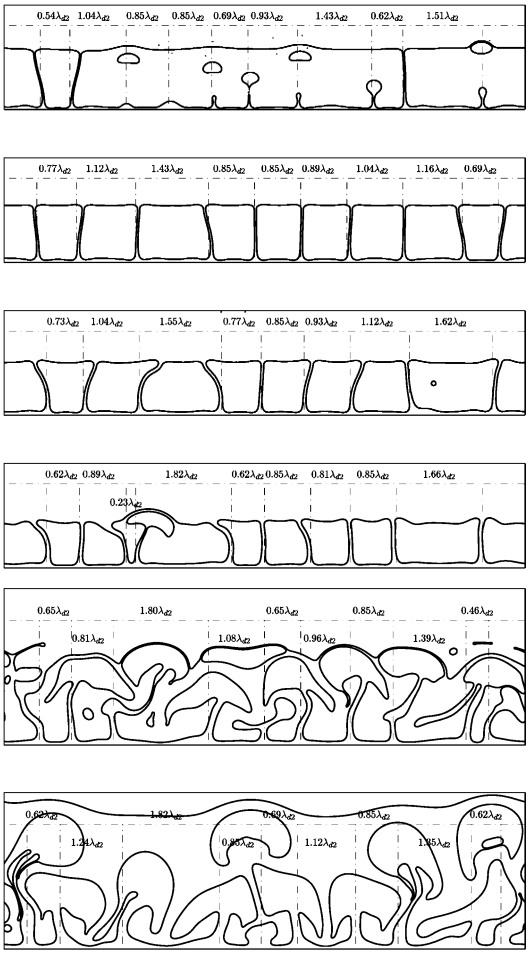

Fig. 8. Comparison of the phase boundaries for multimode simulations at Jacob numbers 0.0640, 0.213, 0.427, 0.853, 2.132, and 10.66. The frame proceeds from the top to the bottom. The time is 181.26 for the first four frames, 44.62 for the fifth frame, and 31.37 for the last frame.

between the vapor in the film and the vapor in the upper layer once they coalesce with the top interface. Three such bridges can be seen, for example, in the first frame. Frame by frame investigations of the interface evolution for the last two runs showed that some of the jets may break in the middle, possibly due to a Kelvin–Helmholtz instability. The investigations also showed interactions between the jets. Comparison of this figure with Fig. 7 shows a decrease in the height of the liquid pool. This is due to liquid evaporation. If any of these simulations are continued indefinitely, eventually all the liquid will evaporate.

To evaluate the effect of the the unit cell size (i.e, $W$), we also performed a few simulations in smaller domains. In agreement with our earlier observation, we observed that the quasi steady-state Nusselt number was not dramatically affected by a change of the unit cell size.

In Fig. 9 we present some results for the statistically steady-state. Each point on each curve corresponds to an ensemble average over runs at different unit cells. The first frame of the figure shows $\overline{\langle Nu \rangle}$ as a function of $Ja$ along with the predictions of Berenson and Klimenko. Since in these simulations bubbles were released mostly from the same location, we have reduced the lead constant in Eq. (1) from 0.425 to 0.36 (as proposed by Dhir et al. [7]). The figure shows a good agreement between the quasi steady-state Nusselt number and the (modified) Berenson's relation while the Klimenko's correlation underpredicts the results. It is seen that the rate of change of $\overline{\langle Nu \rangle}$ with $Ja$ decreases at Jacob number larger than one. This is consistent with the Klimenko's correlation which suggest that $\overline{\langle Nu \rangle}$ is independent of $Ja$ for $Ja > 0.71$. We note that Berenson's correlation slightly underpredicted Son and Dhir's [11] results for film boiling near critical pressure while Klimenko's correlation overpredicted their results by up to 52%. The second frame of Fig. 9 shows $\tilde{\tau}$ as a function of the Jacob number along with the (modified) Zuber's predictions. The numerical period is ensemble averaged over several cycles for $Ja \leqslant 0.0640$ where bubbles were continuously released. Since the vapor jets did not break up beyond $Ja = 0.0640$, the bubble period for $Ja > 0.0640$ was estimated by measuring the time it took for the formation of the first set of bubbles. This, however, leads to an underprediction of the period for $Ja > 0.0640$, since the first bubble release period is usually shorter than the quasi steady-state one due to a large initial temperature gradient at the phase boundary in the vapor side. The figure shows a decline in bubble release period as the Jacob number is increased, in agreement with our earlier analysis where we showed that $\tilde{\tau} \sim Ja^{-3/4}$. Chang's correlation, on the other hand, results in values that are substantially different from our results and also predicts $\tilde{\tau} \sim Ja^{-1/3}$.

A conservative estimate of the film thickness $\delta$ (i.e., ignoring the phase change) can be obtained from an energy balance at the wall, $-k_v \partial T/\partial y = h\Delta T$, $h$ being the heat transfer coefficient. If the temperature gradient is approximated by $\Delta T/\delta$, the energy balance results in $\delta \simeq k_v/h$ and nondimensionalization leads to $\tilde{\delta} \simeq 1/Nu$, where $\tilde{\delta} = \delta/l_s$ and $Nu = hl_s/k_v$. While static models such as Berenson's assume $\delta$ to be uniform, $\delta$ is not uniform and continuously evolves, as we have already observed. Single-mode simulations showed that the film thickness was initially minimum at the sides of the wall as a result of the initial perturbation, but the minimum moved toward the vapor dome during the bubble formation. Fig. 9c shows $\tilde{\delta}$ versus $Ja$ for single-mode simulations. The numerical values were obtained by measuring the maximum and the minimum film thickness over equi-interval times at steady-state and taking the ensemble average of the results. The theoretical values were found using $\tilde{\delta}_B = 1/Nu_B$ and $\tilde{\delta}_K = 1/Nu_K$.

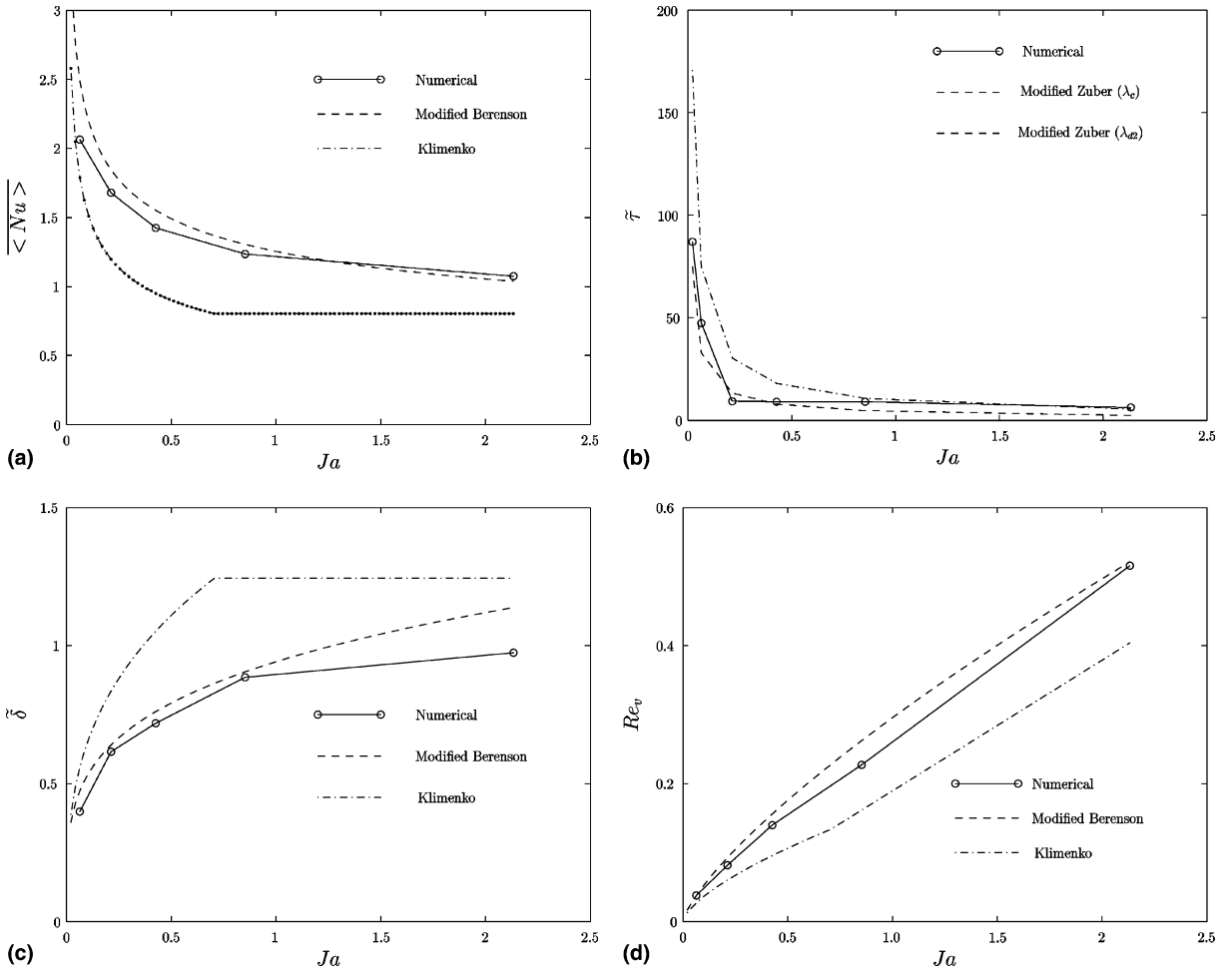


Fig. 9. (a) Quasi steady-state Nusselt number (b) bubble release period, (c) film thickness, and (d) nondimensional vapor velocity as a function of the Jacob number.

The vapor generation rate increases with increase in the wall superheat. We can get an estimate of the dependency of the vapor velocity on the wall superheat using a simple energy balance at the phase boundary; $-k_v \partial T/\partial y|_v = \rho_v(v_v - v_f)h_{fg}$, where $v_v = \bar{v}_v \cdot \bar{n}$ and $v_f = \bar{v}_f \cdot \bar{n}$. Here, $\bar{n}$ is a unit normal velocity at the phase boundary, $v_v$ is the vapor velocity at the phase boundary and $v_f$ is the velocity of the phase boundary. If we approximate $-\partial T/\partial y|_v \simeq \Delta T/\delta$, then $v_v - v_f \simeq k_v \Delta T/\delta \rho_v h_{fg}$. Nondimensionalization leads to $Re_v \simeq Ja/(Pr\tilde{\delta})$, where $Re_v = \rho_v(v_v - v_f)l_s/\mu_v$. Substitution for $\tilde{\delta}$ in terms of $Nu$ using Eq. (1) results in $Re_{v,B} \simeq 0.425(Ja^3 Gr/Pr^3)^{1/4}$. A similar relation can be found using Eq. (2). The fourth frame of Fig. 9 shows the variation of $Re$ with $Ja$. The numerical results were obtained by computing the temperature gradient at the phase boundary. The figure shows a good agreement between the numerical results and the analytical estimate based on Eq. (1).

### 3.5. Effect of the Grashof number

In the simulations presented so far, we used $Gr = 17.85$ (instead of $Gr = 36 \times 10^4$ for water at $p = 0.765 p_c$) to avoid resolving an extremely thin vapor film on the wall. To evaluate the effect of this parameter on our results, we have run a multimode simulation at $Gr = 446$ and a few single-mode simulations at higher $Gr$. These simulations were done by reducing the viscosity and the heat conductivity of both phases. As a result, the characteristic length, time, and velocity scales were not affected. Berenson's and Klimenko's correlations predict $Nu \sim Gr^n$, where $n = 1/4$ and $1/3$, respectively. Since $\tilde{\delta} \simeq 1/Nu$, then $\tilde{\delta} \sim 1/Gr^n$. Therefore, an order of magnitude increase in $Gr$ leads to about 50% reduction in the film thickness. This translates to the necessity for a twofold increase in the grid resolution. As a result, as the Grashof number increases, using a uniform grid

becomes more and more expensive. While we simulated the $Gr = 446$ case using a uniform grid of 256 grid points per $\lambda_{d2}$, we used a nonuniform grid (where we clustered the grids together in the film) to simulate a few single-mode flows at $Gr > 446$. The grid resolutions outside the film and in the horizontal direction were comparable with the uniform grid resolution used earlier. All the simulations reported in this section were done at $Ja = 0.064$ which is the same as that of Fig. 3.

Fig. 10 shows a few frames from the multimode simulation in a $\widetilde{W} = 10$ cell. Here, the first five frames are at transient times and the last frame is at a quasi steady-state time. It is seen that the average bubble spacing for the first set of bubbles is close to what we observed for the low Grashof number flows. The bubbles, however, are more deformed and rise faster. Compared to the low Grashof number simulations, no steady jet is formed, the vapor threads are shorter, and the vapor film is also thinner.

In Fig. 11 we plot $\overline{\langle Nu \rangle}$ as a function of $Gr$ for a few single-mode simulations along with Berenson's and Klimenko's correlations. While the agreement between Berenson's prediction and our result is good, Klimenko's correlation lead to an overprediction. We also measured the quasi steady-state bubble release period for these runs. Eq. (4) predicts $\tilde{\tau} \sim Gr^{-1/4}$ at a fixed wall superheat. However, since in the simulations presented here both $Gr$ and $Re$ are changed (Table 3), in Fig. 11b we plot $\tilde{\tau}/Re$ as a function of $Gr$ to account for variations of $Re$. Notice that although $Ja$ is fixed for these simulations, $Ja_{\min}$ does not remain the same as $Gr$ changes

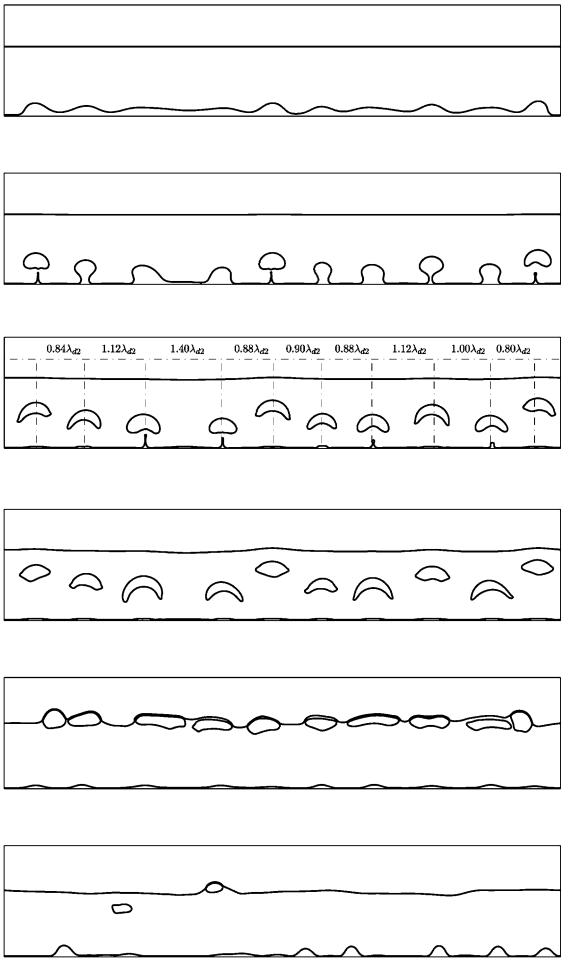


Fig. 10. Evolution of a multimode phase boundary at $Ja = 0.064$. The initial interface consists of $N = 30$ random waves in a $10\lambda_{d2} \times 2\lambda_{d2}$ domain. The grid resolution is $2560 \times 512$. Here, except for $Gr = 446$, all the other nondimensional numbers are the same as the corresponding ones in Fig. 3. The frames proceed from the top to the bottom and times are 10.46, 16.03, 20.22, 23, 34.86, and 76.

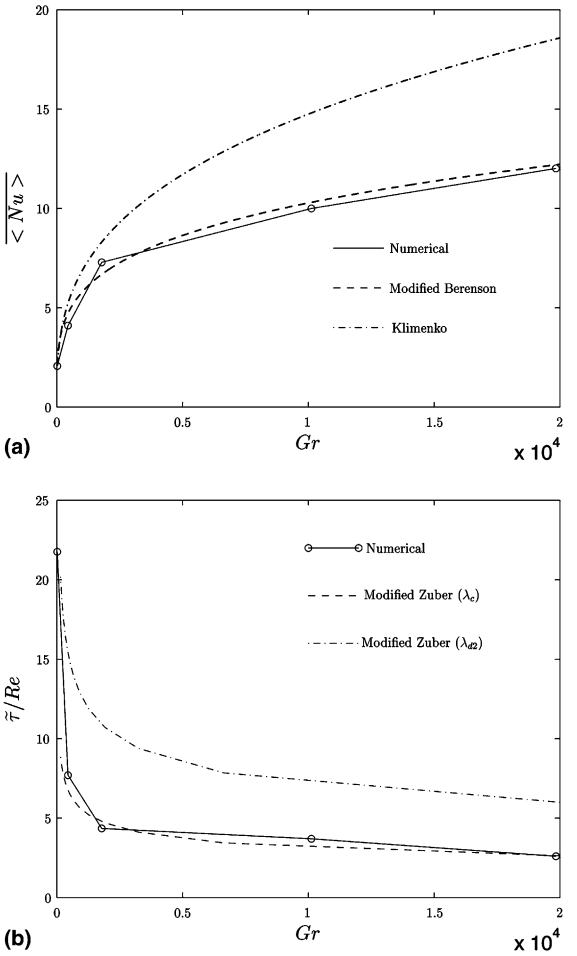


Fig. 11. Evolution of quasi steady-state (a) Nusselt number and (b) (scaled) bubble release period as a function of $Gr$. The results correspond to single-mode simulations in $\lambda_{d2} \times 2\lambda_{d2}$ domains.

Table 3
Variation of $Re$ and $Ja_{\min}$ with $Gr$

| $Gr$ | $Re$ | $Ja_{\min}$ |
|---|---|---|
| 17.85 | 2.173 | 0.4375 |
| 446 | 10.866 | 1.2793 |
| 1785 | 21.732 | 2.0308 |
| $10^4$ | 51.743 | 3.6210 |
| $2\times10^4$ | 72.44 | 4.5316 |

(Table 3). Thus, the analytical period has been modified by $\tilde{\tau}_o = \tilde{\tau}_{\min}(Ja_{\min}/Ja_o)^{3/4}$. It is seen that both the numerical period and the modified Zuber's period show a similar trend and also the Zuber's period based on $\lambda_c$ correlates better with our results.

To investigate the sensitivity of the results to the size of the unit cell, we also ran another simulation at $Gr = 446$ in a $\widetilde{W} = 2$ cell. A plot of $\overline{\langle Nu\rangle}$ and $\tilde{\tau}$ as a function of $\widetilde{W}$ showed that, as before, the results are essentially independent of the unit cell size. In summary, we believe that based on the simulations for two-dimensional systems, the major observations made in this study for the low Grashof number flows carry over for higher Grashof numbers. This, however, needs to be verified by simulating three-dimensional systems.

## 4. Conclusion

Film boiling on horizontal walls was studied by direct numerical simulation. Effect of the unit cell size and the number of initial perturbation waves on the results was studied by simulating two- and three-dimensional systems. The three-dimensional systems, simulated in small domains and for a relatively short periods, showed the possibility of bubble spacings less than most unstable three-dimensional wave length $\lambda_{d3}$. The two-dimensional systems, simulated in large domains and for long times, showed a distribution of bubble spacing. The evolution of the Nusselt number and bubble release period as a function of unit cell size showed that these quantities are essentially independent of the unit cell size. Comparison of the statistically steady-state Nusselt numbers with the (modified) Berenson's prediction at different wall superheats showed a very good agreement. The effect of Grashof number was studied and it was shown that the observations made for the low Grashof number flows, such as the average bubble spacing and the effect of the unit cell size, may still hold.

## Acknowledgment

This work was supported by NASA Microgravity program under grant numbers NAG3-2162 and NAG3-2583.

## References

[1] A. Esmaeeli, G. Tryggvason, Computations of film boiling. Part I-Numerical Method, in press.
[2] N. Zuber, On the instability of boiling heat transfer, Trans. ASME 80 (1958) 711–720.
[3] P.J. Berenson, Film Boiling heat transfer from a horizontal surface, J. Heat Transfer 83 (1961) 351–358.
[4] V.V. Klimenko, Film boiling on a horizontal plate-new correlation, Int. J. Heat Mass Transfer 24 (1981) 69–79.
[5] V.V. Klimenko, A.G. Shelepen, Film boiling on a horizontal plate-a supplementary communications, Int. J. Heat Mass Transfer 25 (1982) 1611–1613.
[6] R.E. Hosler, J.W. Westwater, Film boiling on a horizontal plate, ARS J. 32 (1962) 553–558.
[7] V.K. Dhir, J.N. Castle, I. Catton, Role of Taylor instability on sublimation of a horizontal slab of dry ice, J. Heat Transfer 99 (1977) 411–418.
[8] P.Y. Chang, Wave theory of heat transfer in film boiling, J. Heat Transfer 81 (1959) 1–12.
[9] J.H. Lienhard, V.K. Dhir, On the prediction of the minimum pool boiling heat flux, the minimum pool boiling heat flux, J. Heat Transfer 102 (1980) 457–460.
[10] J.H. Lienhard, K.-H. Sun, Effect of gravity and size upon film boiling from horizontal cylinders, Trans. ASME 92 (1970) 292–298.
[11] G. Son, V.K. Dhir, Numerical simulation of film boiling near critical pressures with a level set method, J. Heat Transfer 120 (1998) 183–192.
[12] S.G. Yiantsios, B.G. Higgins, Rayleigh–Taylor instability in this viscous films, Phys. Fluids A 1 (1989) 1484–1501.
[13] T.D. Hamill, K.J. Baumeister, Film boiling heat transfer from a horizontal surface as an optimal boundary value process, Proc. 3rd Int. Heat Trans. Conf. 4 (1966) 59–64.
[14] E. Abadzic, R.J. Goldstein, Film boiling and free convection heat transfer to carbon dioxide near the critical state, Int. J. Heat and Mass 13 (1970) 1163–1175.
[15] G. Son, V.K. Dhir, N. Ramanujapu, Dynamics and heat transfer associated with a single bubble during nucleate boiling on a horizontal surface, ASME J. Heat Transfer 121 (1999) 623–631.